# The Field Distributions and Balances in a Baroclinic Annulus Wave

**GARETH P. WILLIAMS**—*Geophysical Fluid Dynamics Laboratory,*[1] *NOAA, Princeton, N.J.*

**ABSTRACT**—The detailed structure of a steady wave occurring in a rotating annulus of square cross-section and having a free surface is presented. The field distributions are obtained by numerical integration of the three-dimensional nonlinear Navier-Stokes equations.

The distributions of pressure, temperature, and the three velocity components are displayed for the total fields and for the fields of deviation from the zonal means. Their dynamical balances are also discussed. The deviation wave is a type of Eady wave and the solution is used to discuss the structure of such waves in finite amplitude steady-state form under the influence of variations in baroclinicity, shear, and boundary layers.

The side layers make little contribution to the characteristics of the wave in the deviation field although significant Ekman layer features do appear. The flow is essentially in hydrostatic and geostrophic balance except in the boundary layers. Heat conduction is important only in the side layers.

## 1. INTRODUCTION

The modern picture of the motions of the earth's atmosphere began with the acquisition in the 1940s of details of the motions in the upper atmosphere. These and subsequent studies showed that large-scale eddies, cyclones, and anticyclones play an essential role in the maintenance of the global circulation against frictional dissipation. These eddies are associated with large-scale traveling waves in the westerly winds of midlatitudes. An understanding of the existence and character of waves with the same properties as those observed is a major problem in forming an understanding of the global circulation.

The emergence of a consistent theory for the global circulation began primarily with the identification by Charney (1947) and Eady (1949) of the baroclinic instability mechanism. This mechanism produced a wave motion indicative of cyclone waves in the atmosphere. The theory of baroclinic instability is now central to our understanding of the dynamics of the atmosphere.

The continuing development of the theory of baroclinic instability takes many forms. One of the most informative approaches has been the linearized perturbation method for small amplitude waves. This approach has mathematical difficulties and was limited initially to an examination of waves with simple basic states. Since then, notable developments have included (1) Barcilon's (1964) study of the effects of Ekman layers upon baroclinic waves, (2) Pedlosky's (1964) use of the two level model to examine the effect of lateral shear, and (3) McIntyre's (1970) study of small lateral shear effects on the Eady problem. Most of these studies have been concerned with infinitesimal disturbances of the basic flow and are thus of limited application to global atmospheric dynamics. To extend the theory toward greater realism, one must examine baroclinic waves as they develop into finite amplitude waves

and become affected by nonlinear processes. Pedlosky (1970) has begun studies in this direction for the two-layer model, but the remaining problems are formidable.

Another approach toward the study of baroclinic waves developed after Hide (1953) showed that waves could be produced in the annulus convection experiments. The experiments showed that the flow types occurring in the system fell into four categories: axisymmetric, steady wave, vacillating wave, and irregular motions. Experimental determinations of the occurrence of the different flow regimes have been accumulated.

The annulus waves were hypothesized by Lorenz (1956) to be baroclinic waves and subsequent theoretical studies to explain the complex regime diagrams (e.g. Lorenz 1962, 1963, Barcilon 1964) were based on this hypothesis. These analyses have made an important contribution by their classification of various types of baroclinic waves. The experimental difficulties of measuring the internal details of these waves have never been really overcome. Thus experimental and theoretical interaction has been limited to explaining flow regime transitions, and the experiments have given little information as regards the detailed structure of waves.

The present stage of development of baroclinic instability theory requires that we obtain an understanding of the character of waves under more general basic states, of finite-amplitude waves, and of time-dependent waves. This understanding is necessary if the theory is to develop toward greater applicability to the atmosphere.

The purpose of this paper is to present details of a steady annulus wave as obtained by numerical integration of the three-dimensional Navier-Stokes equations. We study annulus waves because these waves are finite-amplitude baroclinic waves and are formed under conditions of general shear and baroclinicity. Thus, they can provide the details of the character of those waves being sought theoretically and may thus aid in the development and confirmation of such theories. Numerical integration

[1] At Forrestal Campus of Princeton University.

is necessary to provide the details of the waves because of the difficulties in observing the pressure and velocity fields. It is also hoped that presentation of flow details will help in the development of observational methods as well as in providing an example for theoretical analysis.

The numerical solution does confirm the validity of Lorenz' hypothesis as to the nature of the waves (Williams 1971). We will also see that the annulus deviatoric wave fields are reasonably free of the influence of those complex features peculiar to the annulus system such as the side boundary layers.[2] Because of this, the experiments provide relevant data for baroclinic instability theory.

## 2. THE PREDICTION EQUATIONS AND PARAMETER VALUES

We will consider the motion of a fluid bounded by two coaxial cylinders of inner and outer radii, $a$ and $b$, respectively, and two parallel horizontal planes which are a distance, $d$, apart (fig. 1A). The container rotates at a uniform rate, $\Omega$, where the rotation vector, antiparallel to gravity, $g$, coincides with the vertical axis of the cylinders. Motion relative to the solid rotation of the container is measured in cylindrical coordinates, $r$, $\phi$, and $z$, with $r$ being the radial axis and $z$ the vertical axis. The velocity components are $u$, $v$, and $w$ in the zonal, radial, and vertical directions, respectively. The angular size of the annulus sector, $\Phi$, is normally $2\pi$ but for the calculations we consider only the sector $\Phi = 2\pi/5$ (fig. 1B), for reasons discussed in Williams (1971).

The following definition of a Boussinesq liquid is taken for convenience: a liquid in which density variations are negligible except in the buoyancy term and in which the coefficients, $\nu$, $\kappa$, and $\beta$, of viscosity, heat diffusivity, and thermal expansion, respectively, are constant. We also take the centrifugal acceleration to be negligible compared with gravity; that is, $\Omega^2 b/g \ll 1$. As a consequence, the upper surface can be taken to be of constant height and the free-slip rigid lid condition can be used for this surface.

The perfectly conducting inner and outer cylinders are held at different constant temperatures, $T_a$ and $T_b$, respectively. This imposed horizontal temperature differential, $\Delta T = T_b - T_a$, drives the fluid away from a state of solid rotation. The base and upper surface are thermally insulating.

Upon writing the hydrostatic pressure deviation as $\pi = p/\rho_0$ and the temperature deviation from $T_a$ as $T$, the Navier-Stokes equations for this system may be expressed in the following form:

$$\frac{Dv}{Dt} = -\pi_r + \left(2\Omega + \frac{u}{r}\right)u + \nu\left(\nabla^2 v - \frac{v}{r^2} - \frac{2u_\phi}{r^2}\right), \quad (1)$$

$$\frac{Du}{Dt} = -\frac{1}{r}\pi_\phi - \left(2\Omega + \frac{u}{r}\right)v + \nu\left(\nabla^2 u + 2\frac{v_\phi}{r^2} - \frac{u}{r^2}\right), \quad (2)$$

and

$$\frac{Dw}{Dt} = -\pi_z + \beta g T + \nu\nabla^2 w, \quad (3)$$
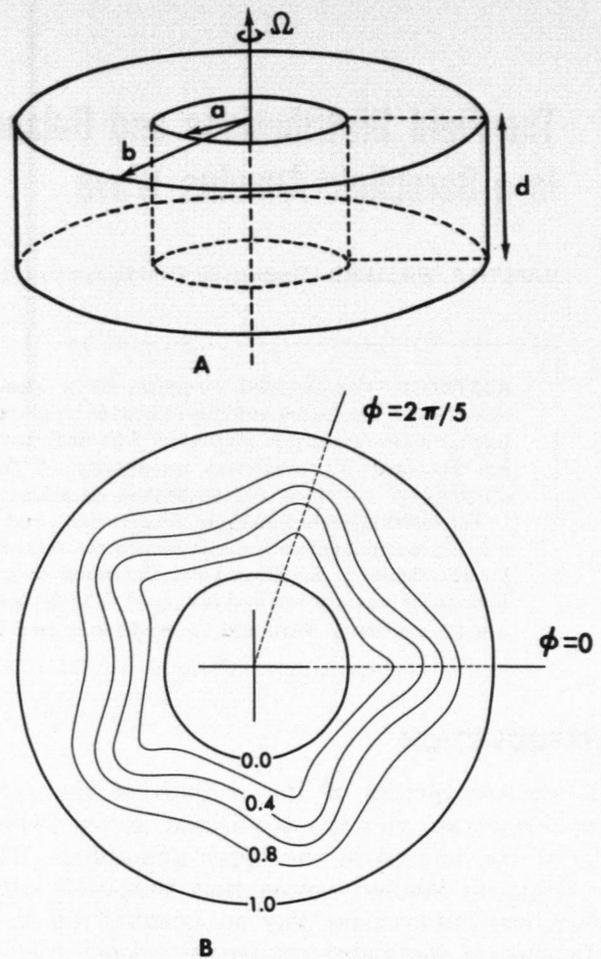
FIGURE 1.—(A) configuration of the system and (B) pressure wave at the upper surface. The container rotates counterclockwise at $\Omega = 0.8$ rad/s and the wave rotates counterclockwise relative to the container at $\Omega^* = 0.033$ rad/s. Domain of interest is $\phi = 0°-72°$. The pressure is normalized in terms of the maximum and minimum values, which are 1.8319 and 0.6974 cm²·s⁻².

with the heat transfer equation as

$$\frac{DT}{Dt} = \kappa\nabla^2 T, \quad (4)$$

and the equation of mass conservation as

$$(rv)_r + u_\phi + rw_z = 0, \quad (5)$$

where we have defined the operator identities

$$\frac{Dq}{Dt} \equiv q_t + vq_r + \frac{u}{r}q_\phi + wq_z \quad (6)$$

and

$$\nabla^2 q \equiv q_{rr} + \frac{1}{r}q_r + \frac{1}{r^2}q_{\phi\phi} + q_{zz}. \quad (7)$$

The boundary conditions as used in the calculations and which express the state of the fluid at the boundaries are:

$$w = v = u = T_z = 0, \quad \pi_z = \beta g T + \nu w_{zz} \quad (8)$$

on the base,

$$w = v_z = u_z = T_z = 0, \quad \pi_z = \beta g T \qquad (9)$$

on the free surface,

$$w = v = u = 0, \quad \pi_r = \nu \left( v_{rr} + \frac{v_r}{r} \right) \qquad (10)$$

on the side walls, and $T = 0$, $\Delta T$, applied at $r = a, b$, respectively. We assume periodicity in $\Phi$.

The finite-difference procedure for solving the system of eq (1)–(10) is given in Williams (1969). The parameter values used in the calculation to give a steady wave are listed below.

    1. Geometry

$$a = 2 \text{ cm}, \ b = 5 \text{ cm}, \ d = 3 \text{ cm}.$$

    2. Physical Properties (water at 20° C)

$$\nu = 1.008 \times 10^{-2} \text{ cm}^2/\text{s}, \ \kappa = 1.420 \times 10^{-3} \text{ cm}^2/\text{s},$$
$$\beta = 2.054 \times 10^{-4} \ (°C)^{-1}.$$

    3. Resolution

$$\Delta r' = 1/32, \ \Delta z' = 1/32, \ \Delta \phi' = 1/36.$$

    4. Nondimensional Numbers

Thermal Rossby number $\pi_4 \equiv \beta g \Delta T d / \Omega^2 \ (b-a)^2 = 0.525$, Taylor number $\pi_5 \equiv 4\Omega^2 \ (b-a)^5/\nu^2 d = 2.041 \times 10^6$, and coordinates $r' = (r-a)/(b-a)$, $z' = z/d$, $\phi' = \phi/\Phi$.

Reasons for this choice of parameters are given in Williams (1971).

The transition curve between axisymmetric and wave flow as estimated from observational data is shown in figure 2. The letter H denotes the solution point. Starting from an initial state in which the fluid is in solid rotation and is at a uniform temperature, $T = \Delta T/2$, the equations are integrated until a quasi-steady wave motion is achieved. The fully developed wave reaches equilibrium and rotates uniformly relative to the container at a rate of $\Omega^* = 0.033$ rad/s. For convenience, the solution is taken when the trough of the surface pressure wave is in the $\phi' = 0$ position (fig. 1B). The accuracy aspects of the solution are discussed in the appendix.

## 3. THE TOTAL FIELDS

The total pressure, temperature, and component wind fields are presented in this section. These fields could be observed experimentally and for this reason presentation in this form is desirable. In discussing the solution, it is useful to look at the variables in terms of the zonal mean, ( ‾ ), and deviations therefrom ( )′. The term "deviatoric" is used for the zonal deviation rather than "eddy" because the flow is laminar and has a finite amplitude. This procedure is justified a posteriori by the nature of the solution but need not necessarily be a meaningful procedure for any three-dimensional flow. The character of the zonal mean fields is given in Williams (1971) and is not discussed further in this paper.
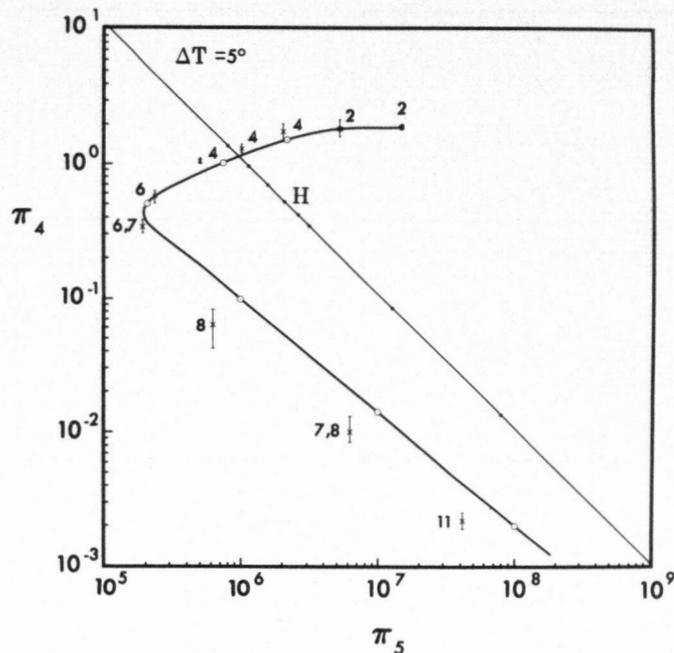


FIGURE 2.—Transition curve between axisymmetric motion (left) and wave motion constructed from data of Fowlis and Hide (1965) for the parameters of the calculation. Coordinates are the thermal Rossby ($\pi_4$) and Taylor ($\pi_5$) numbers. Circled values are from the summary curves of Fowlis and Hide interpreted for our parameter values. Cross marks indicate transition points for observations with small fluid depth (5 cm), and square marks are likewise for small inner radius. Associated wave numbers are given as a guide. The diagonal line $\Delta T = 5°C$ is the locus of interest. The solution is obtained at $H(\Omega = 0.8)$.

The three-dimensional fields are displayed by means of two-dimensional cross-sections. It is convenient to map some of the distributions onto a uniform rectangular area based on the mean length scale of the $\phi$ coordinate. Thus, the geometrical distortion should be borne in mind (cf. figs. 1B, 3E).

### Total Pressure

The pressure wave travels from left to right with the isobars acting as streamlines in the horizontal cross-sections of figure 3. The low-pressure center on the base at $\phi' = \frac{1}{4}$ is associated with the free-surface trough at $\phi' = 0$; this is the characteristic $\frac{1}{4}$ wavelength slope of a baroclinic pressure wave with height. Positive (westerly) zonal flow exists in the upper regions (figs. 3C–3E) whereas negative (easterly) zonal flow occurs in the Ekman layer (fig. 3A). Near the critical level, the flow forms closed circulations (fig. 3B). There are radial variations in the pressure field, but these are more obvious in the deviatoric pressure and will be discussed later.

### Total Temperature

The thermal boundary layers that form along the lower part of the hot outer wall (fig. 4A) and along the upper part of the cold inner wall (fig. 4E) are essentially inde-
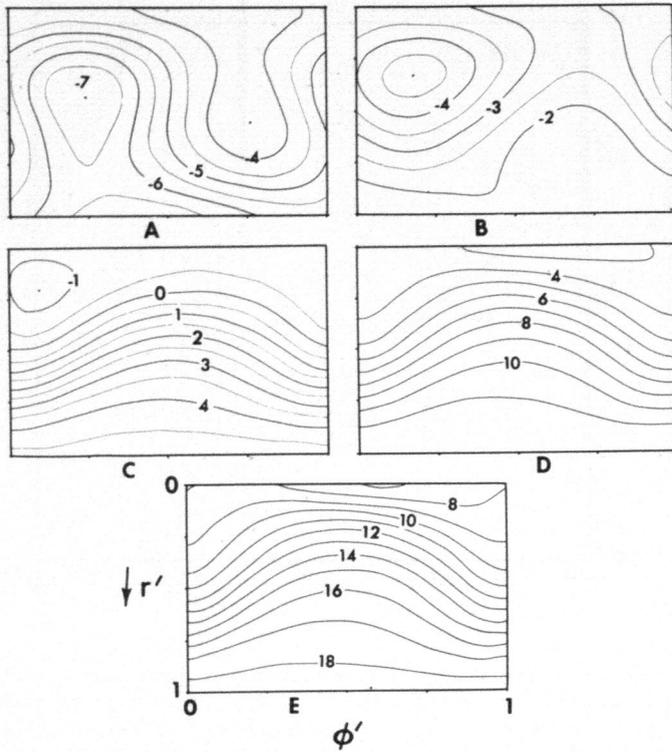
FIGURE 3.—Horizontal sections of total pressure, $\pi$ (units: $10^{-1}$ cm²·s⁻²), at heights of (A) 1/64, (B) 17/64, (C) 33/64, (D) 49/64, and (E) 63/64. Solution is mapped onto a rectangular area. The length of the $\phi'$ abscissa is such that it corresponds to the value at $r' = 1/2$ relative to the radial coordinate length. In each diagram, the cold inner wall is the top boundary. The wave moves from left to right.
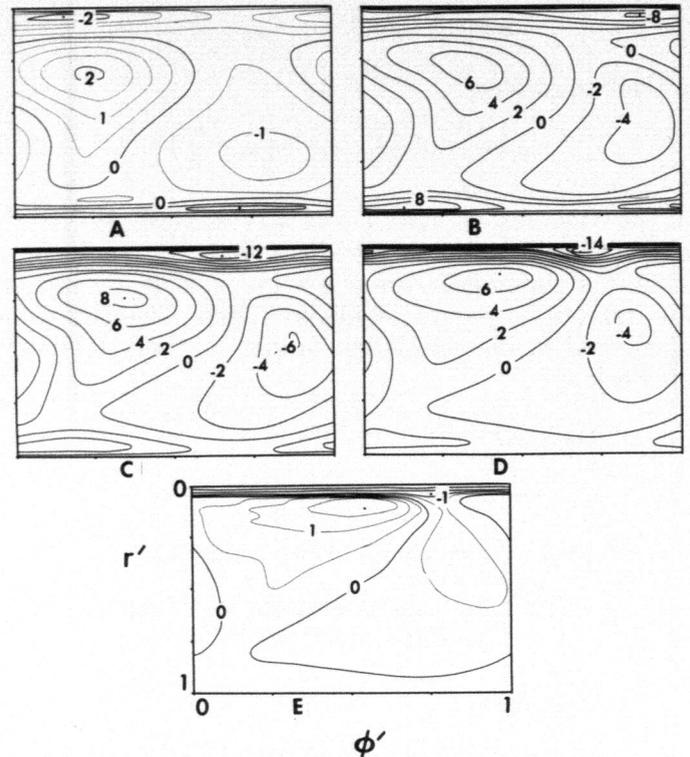
FIGURE 5.—Horizontal sections of vertical velocity, $w$ (units: $10^{-2}$ cm/s), at heights of $z' =$ (A) 2/64, (B) 18/64, (C) 34/64, (D) 50/64, and (E) 62/64. Reduced contour intervals are used in diagrams (A) and (E).
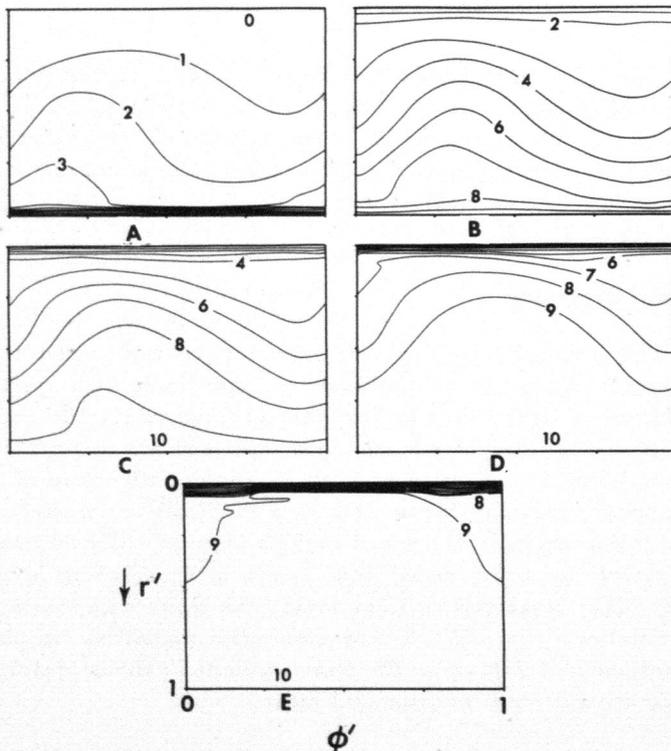
FIGURE 4.—Horizontal sections of normalized temperature, $(T/\Delta T) \times 10$, at heights (A) 1/64, (B) 17/64, (C) 33/64, (D) 49/64, and (E) 63/64.

pendent of $\phi'$. The variation of the temperature, like pressure, is smooth and wavelike.

## Total Vertical Velocity

Separate boundary layer and interior flow regimes exist for the vertical velocity (fig. 5). In the interior region, the flow is predominantly upward as the flow moves inward ($\phi' = 0$–$0.5$) and downward as the flow moves outward, at all heights. Along the side boundaries, there is almost pure boundary layer flow as indicated by the axisymmetry of the isolines. However, some interaction occurs between the interior wave regime and the boundary layer as can be seen in figure 5D where at the cold wall the downflow due to the wave enhances the boundary layer downflow to produce an area of maximum downflow of 0.14 cm/s near $\phi' = 0.75$. The jet leaves the inner wall at this point.

## Total Radial Velocity

The radial velocity contours that we see in figure 6 are produced mainly by the wave motion, as there is only a weak radial velocity associated with the mean fields (see Williams [1971, fig. 4b(i)]). The regions of inflow ($v < 0$) and outflow ($v > 0$) slope backward with height. A geostrophic relation to the isobars (fig. 3) is also apparent.
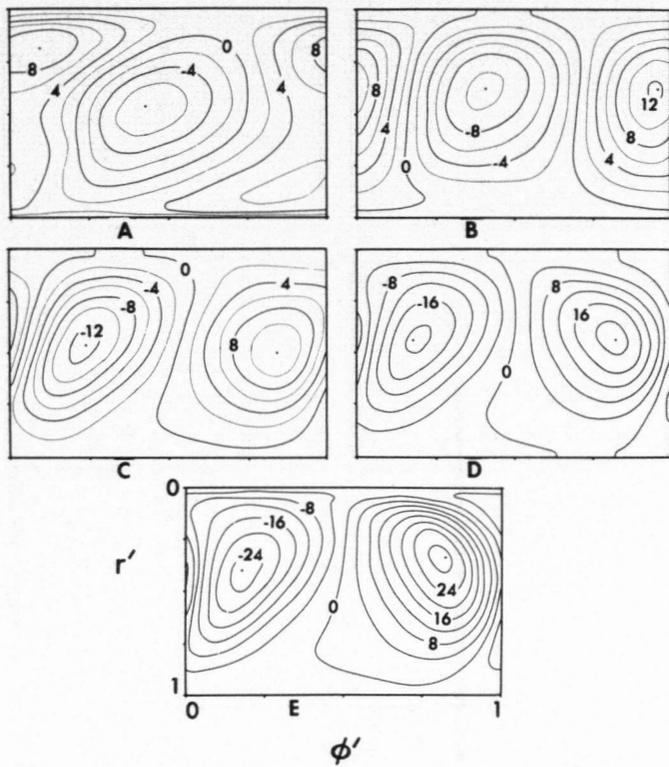
FIGURE 6.—Horizontal sections of radial velocity, $v$ (units: $10^{-2}$ cm/s), at heights of $z' = $ (A) 1/64, (B) 17/64, (C) 33/64, (D) 49/64, and (E) 63/64. A smaller contour interval is used in diagrams (A), (B), and (C).
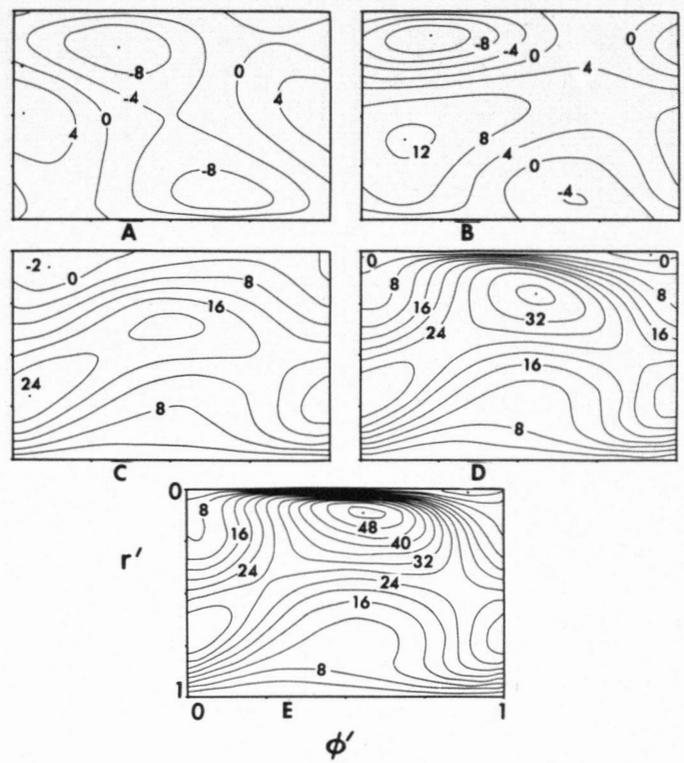


FIGURE 8.—Horizontal sections of zonal velocity, $u$ (units: $10^{-2}$ cm/s), at heights of $z' = $ (A) 1/64, (B) 17/64, (C) 33/64, (D) 49/64, and (E) 63/64.



FIGURE 7.—Vertical sections of zonal velocity, $u$ (units: $10^{-2}$ cm/s), along the wave at $\phi' = $ (A) 0, (B) 10/72, (C) 18/72, (D) 28/72, (E) 36/72, (F) 46/72, (G) 54/72, (H) 60/72, and (I) 64/72 (i.e., 0–1.0 in intervals of approximately 1/8).

## Total Zonal Velocity

The zonal velocity pattern varies considerably along the wave, and it is of interest to examine vertical cross-sections (fig. 7) as well as the horizontal ones (fig. 8). In the trough region (fig. 7A), the jet is nearest the outer wall, its axis is vertical, and the jet magnitude weakest at 0.32 cm/s. With increasing $\phi'$, the jet moves to the inner wall and its axis takes on a diagonal slope. The jet attains a maximum value of 0.52 cm/s at the ridge, $\phi' = 0.5$, and a strong momentum boundary layer forms along part of the top wall (see also fig. 8E). A very small isolated region of negative zonal flow occurs at the upper surface, on the cold wall near $\phi' = 7/8$ (fig. 8E). It is linked to larger regions of negative flow at lower depths (fig. 7A).

## 4. THE DEVIATORIC FIELDS

The deviatoric fields define and reveal the nature of the wave flow more incisively than any other set of variables. Thus, this section will be concerned with discussing the phase and amplitude behavior of the deviatoric fields. This behavior can be represented to a good approximation by two-dimensional quasi-phase, quasi-amplitude diagrams. These may be obtained from the coefficients of the first mode of a Fourier analysis in the $\phi'$ direction and such diagrams are given in Williams (1971, figs. 11 and 12).

FIGURE 9.—Horizontal sections of deviatoric pressure, $\pi'$ (units: $10^{-2}$ cm²·s⁻²), at heights of $z'=$ (A) 1/64, (B) 17/64, (C) 33/64, (D) 49/64, and (E) 63/64. A smaller contour interval is used in diagrams (A)–(C).

FIGURE 10.—Azimuthal sections of deviatoric pressure, $\pi'$ (units: $10^{-2}$ cm²·s⁻²), at radii of $r'=$ (A) 3/64, (B) 17/64, (C) 33/64, (D) 49/64, and (E) 63/64. A smaller contour interval is used in diagrams (A) and (E).

However, we would like in this section to present the nonapproximated form of the deviatoric wave behavior and thence to provide a realization of the complex phase behavior of this quasi-Eady, finite amplitude, steady-state wave with its underlying variable shear, baroclinicity, and boundary layer effects. The nonapproximated form also reveals the extent of nonlinear and higher mode effects not exhibited by the approximated forms.

## Deviatoric Pressure

The deviatoric pressure has a very smooth wavelike behavior (fig. 9). The phase variation can be realized from the zero-value contours with the radial phase variations given by figure 9 and the vertical variations by figure 10. The amplitude behavior is straightforward with largest amplitudes being confined to the central ($r'=0.5$) zone. Low pressure regions have larger amplitudes than the high pressure regions. As regards the interior region of the fluid, the characteristic ¼ wavelength back-slope with height is well established. In the upper one-third of the interior region, the phase varies weakly with height (figs. 10C–10E). The more significant variation occurs in the radial direction with the wave in the middle zone leading those in adjacent regions in the upper half of the fluid [cf. fig. 12, Williams (1971)]. This wave shape is characteristic of angular momentum transfer into the middle zone.

As regards boundary regions, there is a more markedly variable phase behavior than in the interior. Strong radial variations in phase occur near the free surface region of the inner wall where the wave appears to be rapidly retarded (fig. 9E). In the vertical direction, however, the pressure wave on the inner wall has its phase lines leaning backward with height (fig. 10A). The situation is different near the outer wall where the phase variability is mostly a function of height, the phase becoming rapidly horizontal at $z'=0.4$ and sloping forward with height in the lower region (fig. 10E). This indicates the presence of higher wave numbers.

The physical explanation of the phase behavior is unknown and, because of the weak amplitudes near the the sides, the meaningfulness of local phase changes is not established. However, recent studies by Saltzman seem to indicate that such features as phase layering are an inherent property of generalized baroclinic waves.[3] The whole phase behavior is summarized by the quasi-phase diagrams of Williams [1971, fig. 12(a)].

## Deviatoric Temperature

The deviatoric temperature field possesses a certain degree of detail and asymmetry particularly in the sidewall regions (figs. 11 and 12). Although the side

[3] Seminar at the Geophysical Fluid Dynamics Laboratory, NOAA, November 1971
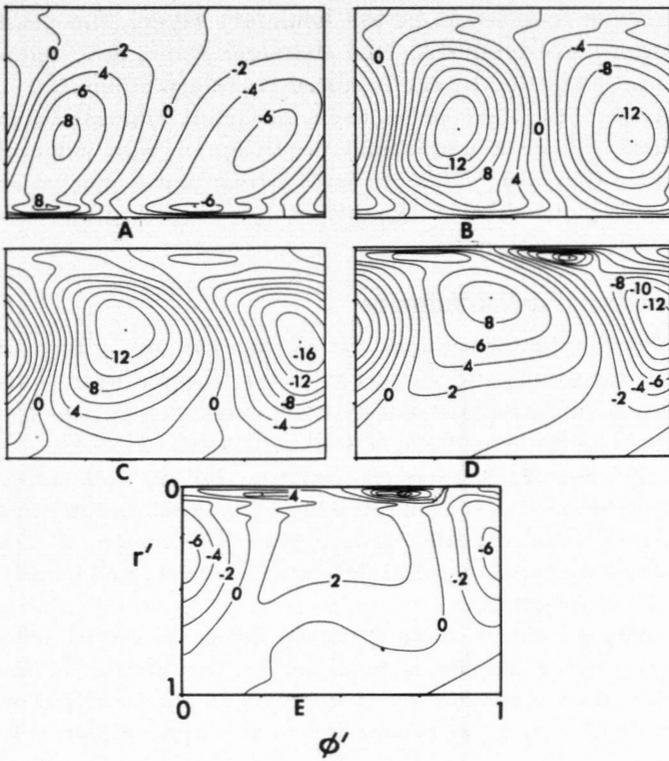
FIGURE 11.—Horizontal sections of deviatoric temperature, $(T'/\Delta T) \times 10^2$, at heights of $z' =$ (A) 1/64, (B) 17/64, (C) 33/64, (D) 49/64, and (E) 63/64.

regions display large phase variability, the associated amplitudes are small. This indicates that thermal boundary layers play only a secondary role in the formation of the deviatoric wave.

In the interior region the phase leans forward with height, a characteristic of the baroclinic wave. The maximum amplitude occurs at midheight.

A region of enhanced cooling occurs near the inner wall near $\phi' = \frac{5}{8}$ (fig. 12A) and is correlated with the maximum downflow region.

## Deviatoric Vertical Velocity

The deviatoric vertical motion is closely related to the deviatoric temperature field with upward motion coinciding with positive temperature anomalies. This produces the vital release of potential energy. Thus, the patterns of figures 13 and 14 closely resemble the temperature patterns (figs. 11, 12). The amplitude asymmetries of the vertical velocity occur predominantly in the inner sidewall region. The maximum upward velocity occurs just ahead of the low pressure area on the base as in atmospheric cyclone systems.

In both the $T'$ and $w'$ fields, it is clear that the wave patterns, although less well ordered, are divided into 2 regimes—the interior and sidelayer systems. Whereas
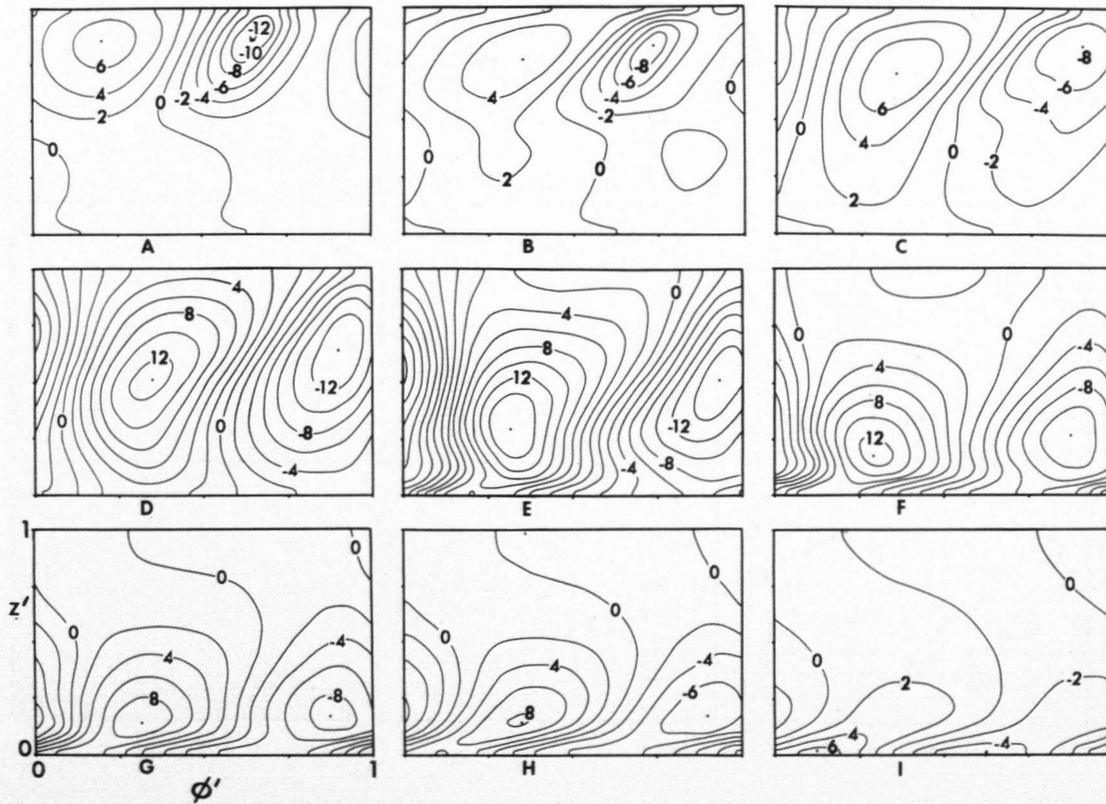


FIGURE 12.—Azimuthal sections of deviatoric temperature, $(T'/\Delta T) \times 10^2$, for (A)–(C), the inner boundary region $r' = 1/64$, 5/64, and 9/64; (D)–(F), the interior region $r' = 17/64$, 33/64, and 49/64; and (G)–(I), the outer boundary region $r' = 55/64$, 59/64, and 63/64.
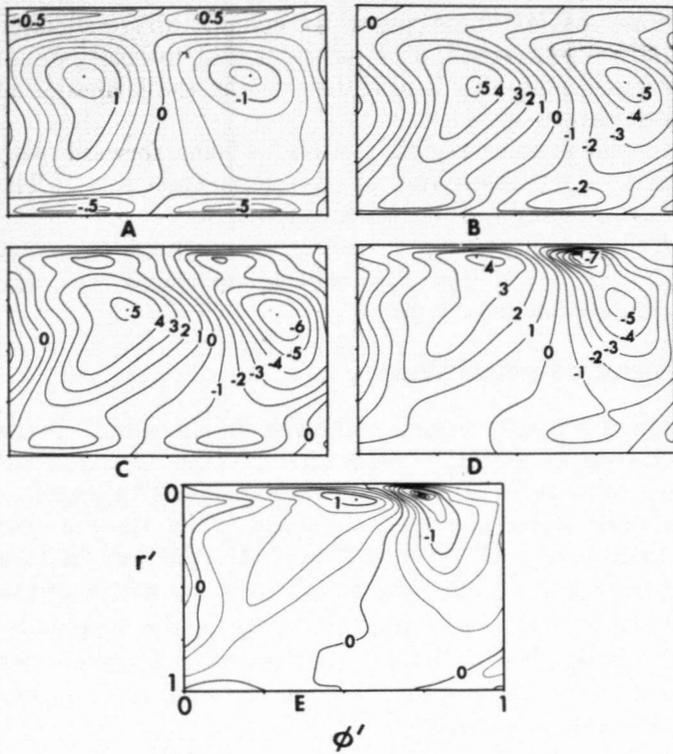
FIGURE 13.—Horizontal sections of deviatoric vertical velocity, $w'$ (units: $10^{-2}$ cm/s), at heights of $z' =$ (A) 2/64, (B) 18/64, (C) 34/64, (D) 50/64, and (E) 62/64. A smaller contour interval is used in diagrams (A) and (E).

the wave is different in the boundary layers, the main interior wave retains its own character and is not fundamentally affected by the localized boundary influences.

At the base there seems to be an almost separate wave system (of weak amplitude) occurring in both sidewall regions (fig. 13A). This produces strong phase changes in those regions. This phenomenon may represent a conservation requirement.

## Deviatoric Radial Velocity

The horizontal sections for $v'$ (fig. 15) are similar to those for total $v$ (fig. 6) except in the Ekman layer. This reflects the fact that $\bar{v}$ is relatively small except near the base. The patterns form a well structured wave similar to the deviatoric pressure pattern (fig. 9) but being approximately ½ wavelength out of phase in the interior regions. This indicates geostrophy. The shape of the velocity wave is somewhat different, however, particularly in the side regions.

Although the $v'$ wave generally leans backward with height, this variation is modified by the Ekman layers which cause a retardation of the wave in the outer region (fig. 16E) and an advancement in the inner region (fig. 16A).

## Deviatoric Zonal Velocity

The phase-amplitude behavior of $u'$ is more difficult to



FIGURE 14.—Azimuthal sections of deviatoric vertical velocity, $w'$ (units: $10^{-2}$ cm/s), for (A)–(C), the inner boundary region $r' = 1/64$, 5/64, and 9/64; (D)–(F), the interior region $r' = 17/64$, 33/64, and 49/64; and (G)–(I), the outer boundary region $r' = 55/64$, 59/64, and 63/64.

FIGURE 15.—Horizontal sections of deviatoric radial velocity, $v'$ (units: $10^{-2}$ cm/s), at heights of $z' =$ (A) 1/64, (B) 17/64, (C) 33/64, (D) 47/64, and (E) 63/64.



FIGURE 17.—Horizontal sections of deviatoric zonal velocity, $u'$ (units: $10^{-2}$ cm/s), at heights of $z' =$ (A) 1/64, (B) 17/64, (C) 33/64, (D) 49/64, and (E) 63/64. A smaller contour interval is used in diagrams (A)–(C).



FIGURE 16.—Azimuthal sections of deviatoric radial velocity, $v'$ (units: $10^{-2}$ cm/s), at radii of $r' =$ (A) 4/64, (B) 18/64, (C) 34/64, (D) 50/64, and (E) 60/64. A smaller contour interval is used in diagrams (A) and (E).

determine than that of other variables because the amplitude vanishes in a transition from positive to negative values near $r' = 0.4$, allowing higher modes to enter in the interior (fig. 17). Apart from this transition zone, the $u'$ pattern is dominated by the first mode. The variable also leans backward with height, indicating a degree of geostrophy in its production (fig. 18).

The maximum amplitude occurs in the free surface jet near the inner wall where momentum boundary layers form along the upper one-fourth of the wall (fig. 17E).

## 5. THE DYNAMICAL BALANCES

To determine how the above wave is produced and maintained dynamically, we conclude with a discussion of some representative diagrams of the component terms of the basic prediction and vertical vorticity equations. The behavior of the terms at $z' = 0.5$ is reasonably representative of the dominant interior and side region balances but further frictional forces enter in the Ekman layer to modify these balances.

### The Vertical Velocity Components

The variation of the components of eq (3) at $z' = 0.5$ and $\phi' = 0$ (fig. 19) indicates that the fluid is in a hydrostatic balance in the interior. The deviation from hydrostatic balance is greater in the side boundary layers than

FIGURE 18.—Azimuthal sections of deviatoric zonal velocity, $u'$ (units: $10^{-2}$ cm/s), at $r' =$ (A) 3/64, (B) 17/64, (C) 33/64, (D) 49/64, and (E) 61/64.



FIGURE 19.—Radial distribution of components of the $w$ equation at midheight ($z' = 33/64$) for $\phi' = -1/72$. Terms are (a) $\beta g T$, (b) $\nu \nabla^2 w$, and (c) $-\pi_z$. Other terms are negligible. Units are cm·s⁻².
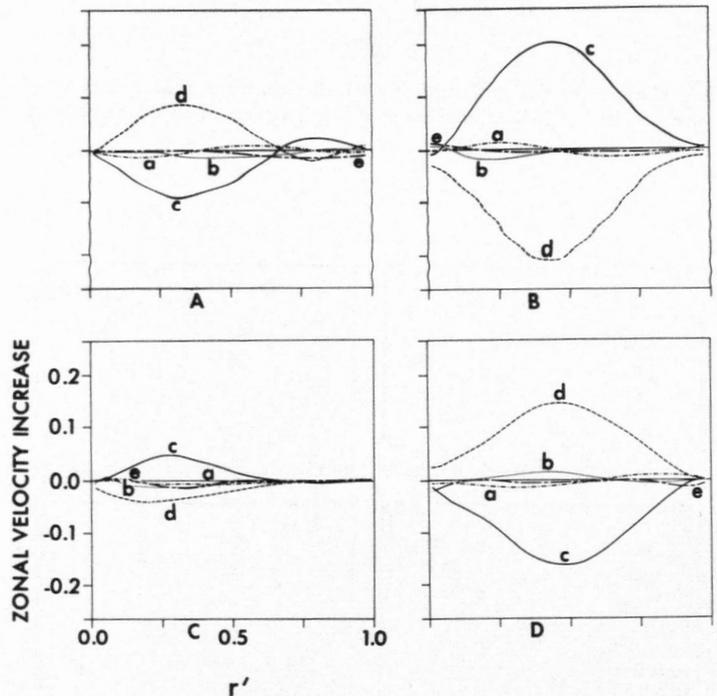


FIGURE 20.—Radial distribution of components of the $u$ equation at midheight ($z' = 33/64$) for $\phi' =$ (A) 0, (B) 18/72, (C) 36/72, and (D) 54/72. Terms are (a) $-u_t$, (b) $-(vu_r + uu_\phi/r + wu_z)$, (c) $-(2\Omega + u/r)v$, (d) $-\pi_\phi/r$, and (e) $\nu \nabla^2 u$. Units are cm · s⁻². Coordinates are all as in (C).

this figure suggests because both layers are relatively weak at $z' = 0.5$. Since the balance varies so slowly with $\phi'$, one diagram is sufficient to show the overall balance

## The Zonal Velocity Components

The representative components of eq (2) for the zonal velocity reveal a predominant balance between the Coriolis term and the pressure gradient at all $\phi'$ values (fig. 20). The $u$ field forms a stronger side boundary layer at $z' = 0.75$ than at this height so the friction term is under-represented. The remaining terms of the equation are smaller but not negligible and will be examined again in the vorticity equation.

## The Radial Velocity Components

The components of eq (1) shown in figure 21 also display a predominant balance between the Coriolis term and the pressure gradient at all $\phi'$. The balances of the $u$ and $v$ equations together form a geostrophic balance so that the isobars can be regarded as streamlines for horizontal flow.

## The Vertical Vorticity Components

The dominance of the geostrophic balance in the $u$ and $v$ equations obscures the balance between the other terms in the two equations. To circumvent this, the equation for

vertical vorticity is formed:

$$\zeta_t + v\zeta_r + \frac{u}{r}\zeta_\phi + w\zeta_z = (2\Omega + \zeta)w_z + \xi w_r + \eta \frac{w_\phi}{r} + \nu\nabla^2\zeta \qquad (11)$$

where

$$\zeta = \frac{1}{r}(ru)_r - \frac{v_\phi}{r}, \quad \xi = \frac{w_\phi}{r} - u_z, \quad \eta = v_z - w_r,$$

are the $(z, r, \phi)$ vorticity components, respectively.
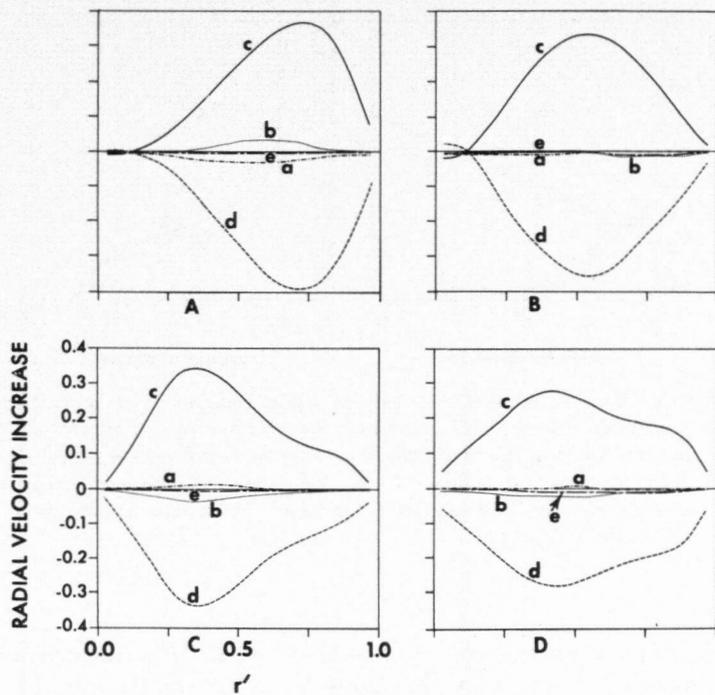
FIGURE 21.—Radial distribution of components of the $v$ equation at midheight ($z' = 33/64$) for $\phi' =$ (A) $-1/72$, (B) $17/72$, (C) $35/72$, and (D) $53/72$. Terms are (a) $-v_t$, (b) $-(vv_r + uv_\phi/r + wv_z)$, (c) $+(2\Omega + u/r)u$, (d) $-\pi_r$, and (e) $\nu\nabla^2 v$. Units are cm $\cdot$ s$^{-2}$. Coordinates are all as in (C).
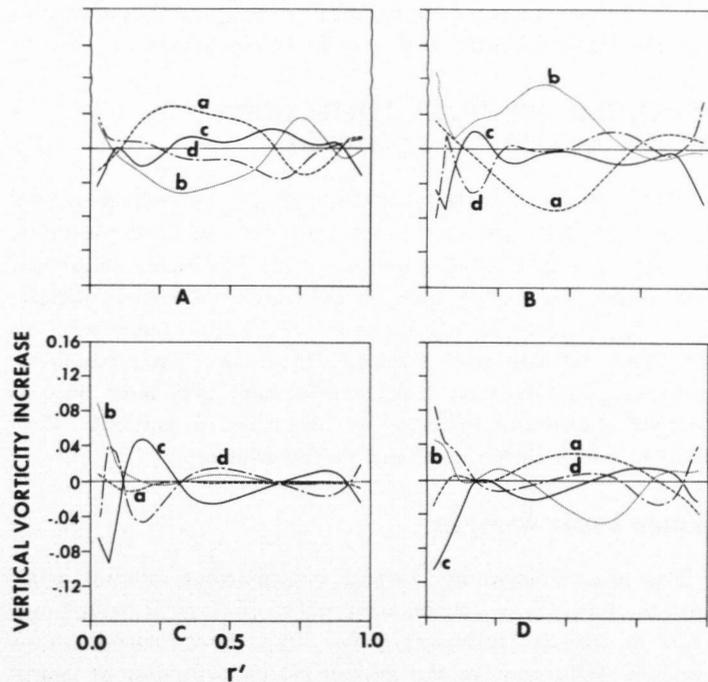


FIGURE 22.—Radial distribution of components of the vertical vorticity ($\zeta = (ru)_r/r - v_\phi/r$) equation at midheight ($z' = 33/64$) for $\phi' =$ (A) 0, (B) 18/72, (C) 36/72, and (D) 54/72. The terms are (a) $-\zeta_t$, (b) $-(v\zeta_r + u\zeta_\phi/r + w\zeta_z)$, (c) $(2\Omega + \zeta)w_z + \xi w_r + \eta w_\phi/r$, and (d) $\nu\nabla^2\zeta$. Units are s$^{-2}$.



FIGURE 23.—Example of the vertical vorticity field, $\zeta$ (units: $10^{-1}$ s$^{-1}$), in three sections: (A) azimuthal section at $r' = 34/64$, (B) vertical section at $\phi' = 0$, and (C) horizontal section at $z' = 33/64$.
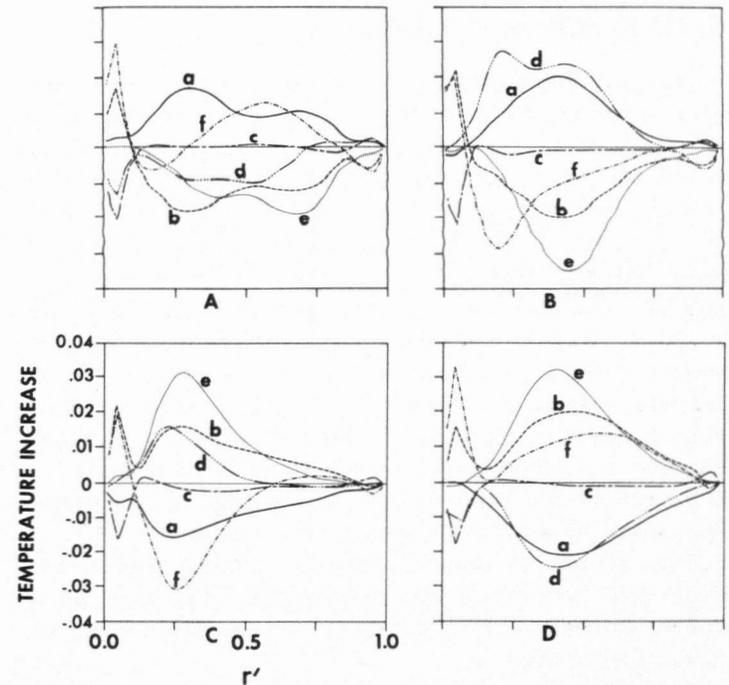


FIGURE 24.—Radial distribution of components of the normalized temperature ($T/\Delta T$) equation at midheight ($z' = 33/64$) for $\phi' =$ (A) $-1/72$, (B) $17/72$, (C) $35/72$, and (D) $53/72$. Terms are (a) $-T_t$, (b) $-(vT_r + uT_\phi/r + wT_z)$, (c) $\kappa\nabla^2 T$, and individual convection terms (d) $-vT_r$, (e) $-uT_\phi/r$, and (f) $-wT_z$. All are normalized by $\Delta T$. Coordinates are all as in (C).

The representative components (fig. 22), do not indicate any predominant balance. An important feature of the balance is the strong viscous term. This is to be expected for we know that in the balances for axisymmetric flow (Williams 1967) the viscous term is large in the balance of the $u$ equation, and $\zeta$ is essentially the gradient of $u$.

Three sections of the vertical vorticity $\zeta$ itself are given in figure 23. Positive spin occurs mainly in the trough

($\phi'=0$) and negative spin mainly near the ridge ($\phi'=0.5$). The positive values have the larger amplitude.

## The Temperature Components

The components of eq (4), the temperature equation, are presented in figure 24. In addition to the three basic terms of the equation, the three component terms of convection are also given separately because each term is important in itself in this predominantly convective flow.

Conduction is negligible in the interior where the balance is between the time term $-T_t$ and the convection term $\mathbf{V} \cdot \nabla T$. In the side boundary layers, the conduction term becomes large whereas the terms $-T_t$ and $uT_\phi/r$ become secondary; this reflects the axisymmetry of the thermal boundary layers. Thus the thermal layer on the inner wall is mainly formed by a balance between the vertical convection term $-wT_z$ bringing warm fluid down the wall and the terms $-vT_r$, $\kappa\nabla^2 T$ removing heat out of the region at $z'=0.5$. The balance of the thermal boundary layers is essentially the same as that of comparable axisymmetric solutions.

## 6. CONCLUDING REMARKS

Detailed characteristics of a steady annulus wave have been presented. The solution provides an indication of the form of steady, finite amplitude, baroclinic waves of the Eady type under the influence of lateral shear and baroclinicity variations and viscosity. A major aspect of the deviatoric fields is the smallness of side boundary layer features which shows that the interior wave is only slightly modified by the side regions. Although the deviatoric wave is essentially a quasi-Eady wave, it does possess some peculiarities of its own as regards phase behavior in boundary regions. This phase behavior still lacks a physical explanation. The phenomenon of phase layering near boundaries could be of consequence in determining the influence of midlatitude disturbances upon tropical ones in the earth's atmosphere.

The dynamical balances of the interior region are essentially hydrostatic and geostrophic. These conditions are in agreement with the usual assumptions made in theoretical studies.

Although the deviatoric wave possesses a certain amount of complexity which makes it difficult to define, it is still possible to define it by means of the quasi-phase, amplitude diagrams given in Williams (1971). A comparison of these diagrams with the field distributions of this paper indicates that this is an accurate procedure. Having been able to "define" the steady wave in this way, we must next consider whether a similar technique will allow us to define the vacillating wave. Clearly, these waves need to be defined, but until a better theoretical basis is established, it will be difficult to provide a thorough analysis of either steady or vacillating waves. The same numerical techniques are appropriate for obtaining the details of vacillating waves, but the problem of defining and analyzing the wave is more difficult. It may be
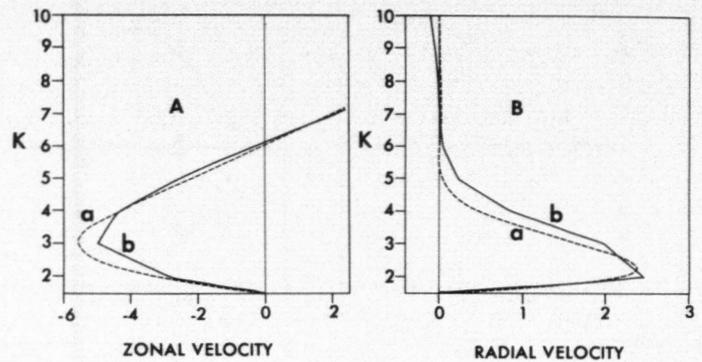


FIGURE 25.—Comparison of (a) an analytical solution and (b) numerical values of the axisymmetric solution at $r'=1/2$ for the Ekman layer on the base. Abscissa scale $10^{-2}$ cm/s and ordinate $K$ indicates the grid points of the numerical scheme that start at one-half grid interval above the base. (A) zonal velocity and (B) radial velocity.

possible to extend the quasi-phase, amplitude diagrams into three-dimensional diagrams by using time as one of the axes.

It is hoped that presentation of field distributions will assist also in the development of observational techniques as has been the case with axisymmetric studies. We have presented a solution at one parameter point only and there remains a need to determine the structure of the flow over the whole regime for wide parameter ranges. Observational studies would be most suitable for this purpose.

## APPENDIX: ACCURACY LIMITATIONS OF THE NUMERICAL SOLUTION

Although the accuracy of the solution presented in this paper cannot be directly evaluated, we can perform analyses that suggest that good accuracy has been achieved. For instance, the axisymmetric solution at the same parameter values may be obtained at the same resolution as the wave solution and at higher resolution. This was done and the solutions were found to be very accurate; that is, integral quantities differed by less than 5 percent. Two further tests will be discussed in this section.

### Ekman Layer Analysis

The most convincing test of a numerical solution that can be made is a comparison with analytical solutions. This is clearly impossible for the complicated wave solution. However, in the axisymmetric solution at point H {see Williams [1971, fig. 4(a)]}, the boundary layer on the base is close to being an Ekman layer at $r'=0.5$ where minimum sidewall and buoyancy effects occur (i.e., $w \approx 0$).

The equations governing the flows at that point are to a good approximation

$$-2\Omega u = -\pi_r + \nu v_{zz}, \qquad 2\Omega v = +\nu u_{zz}. \qquad (12)$$

The boundary conditions are that $u=v=0$ at $z=0$ and

that $v\to0, u\to G$ for large $z$. An analytical solution exists for this problem provided that $G$ is linear in $z$ or constant. As $G$ increases with $z$ {Williams [1971, fig. 4(a)]}, we assume $G$ to be linear in the region just above the Ekman layer. The solution is then

$$u = G(z)(1 - e^{-\gamma} \cos \gamma), \quad v = -G(z)e^{-\gamma} \sin \gamma \quad (13)$$

where $\gamma = z(\Omega/\nu)^{1/2}$ and $G(z) = u_1 z + u_2$. The constants $u_1$, $u_2$ are obtained by matching $G(z)$ with the numerical values of $u$ at the grid points $K=4$ and $7$ (fig. 25)—one point being just inside the layer and one just outside the layer.

The analytical solution (based on two match points) and the numerical solution at $r'=0.5$ are shown in figure 25. The Ekman layer extends up to $K=5$ to $6$ which is consistent with the simple Ekman layer depth formula $\delta = \pi(\nu/\Omega)^{1/2} = 0.35$ cm which is close to $K=5$. The two solutions are close despite the approximation, and it is clear that the numerical solution has adequate resolution for accurate representation of the Ekman boundary layer.

## Resolution and Reynolds Number

The limit of meaningful numerical integration depends on specified resolution. Flows at a higher Reynolds number or of irregular character require higher resolution than flows at lower Reynolds number. We will derive a relationship that gives an idea of the resolution required for accurate solution of flows at a given Reynolds number and, hence, we will show that the wave solution meets the criterion. The criterion for accuracy depends on the choice of finite differencing so as an example we take a simplified equation for $w$ as differenced in the calculation. Using standard central differencing notation, consider the discrete equation

$$\delta_t \overline{w}^t + \overline{\overline{w}^z \delta_z w}^z = \nu \delta_{zz} w. \quad (14)$$

A Taylor expansion gives the continuous form of eq (14) as

$$w_t + w w_z = \left[ \nu - \left( \frac{\Delta z^2}{2} \right) w_z \right] w_{zz} - \left( \frac{\Delta z}{2} \right)^2 w w_{zzz} \quad (15)$$

where for the sake of argument only the truncation terms of the nonlinear term are retained.

For accurate calculation and a proper representation of the inertia-frictional balance in the fluid, the truncation term must be smaller than the friction term (i.e., $R_\Delta \equiv (\Delta z)^2 w_z / \nu \ll 1$). This defines a local grid Reynolds number $R_\Delta$. If the fluid has a bulk Reynolds number $\mathrm{Re} = wd/\nu$, then we can write $R_\Delta/\mathrm{Re} = 1/N^2$ where $N$ is the number of grid points over the length, $d$. If we specify that $R_\Delta = 1/10$ is a sufficient accuracy requirement, then a resolution of $N^2 = 10\,\mathrm{Re}$ must be used. An example would be that, for $\mathrm{Re} = 100$, $N=30$ is required.

The accuracy condition $R_\Delta \ll 1$ is met by the steady wave solution. Although the above criterion is somewhat arbitrary, it does give an idea of the order of magnitude of the resolution. More importantly, the analysis suggests that resolution varies as $\mathrm{Re}^{1/2}$ for a fixed accuracy which is more favorable than varying as $\mathrm{Re}$.

## REFERENCES

Barcilon, Victor, "Role of the Ekman Layers in the Stability of the Symmetric Regime Obtained in a Rotating Annulus," *Journal of the Atmospheric Sciences*, Vol. 21, No. 3, May **1964**, pp. 291–299.

Charney, Jule G., "The Dynamics of Long Waves in a Baroclinic Westerly Current," *Journal of Meteorology*, Vol. 4, No. 5, Oct. **1947**, pp. 135–162.

Eady, E. T., "Long Waves and Cyclone Waves," *Tellus*, Vol. 1, No. 3, Stockholm, Sweden, Aug. **1949**, pp. 33–52.

Fowlis, W. W., and Hide, R., "Thermal Convection in a Rotating Annulus of Liquid: Effect of Viscosity on the Transition Between Axisymmetric and Non-Axisymmetric Flow Regimes," *Journal of the Atmospheric Sciences*, Vol. 22, No. 5, Sept. **1965**, pp. 541–558.

Hide, Raymond, "Some Experiments on Thermal Convection in a Rotating Liquid," *Quarterly Journal of the Royal Meteorological Society*, Vol. 79, No. 339, London, England, Jan. **1953**, p. 161.

Lorenz, Edward N., "A Proposed Explanation for the Existence of Two Regimes of Flow in a Rotating Symmetrically-Heated Cylindrical Vessel," *Proceedings of the First Symposium on the Use of Models in Geophysical Fluid Dynamics, Johns Hopkins University, Baltimore, Maryland, September 1-4, 1953*, Office of Naval Research and U.S. Weather Bureau, Washington, D.C., **1956**, pp. 73–80.

Lorenz, Edward N., "Simplified Dynamic Equations Applied to the Rotating-Basin Experiments," *Journal of the Atmospheric Sciences*, Vol. 19, No. 1, Jan. **1962**, pp. 39–51.

Lorenz, Edward N., "The Mechanics of Vacillation," *Journal of the Atmospheric Sciences*, Vol. 20, No. 5, Sept. **1963**, pp. 448–464.

McIntyre, M. E., "On the Non-Separable Baroclinic Parallel Flow Instability Problem," *Journal of Fluid Mechanics*, Vol. 40, No. 2, Cambridge, England, Feb. **1970**, pp. 273–306.

Pedlosky, Joseph, "The Stability of Currents in the Atmosphere and the Ocean: Part I," *Journal of the Atmospheric Sciences*, Vol. 21, No. 2, Mar. **1964a**, pp. 201–219.

Pedlosky, Joseph, "The Stability of Currents in the Atmosphere and the Ocean: Part II," *Journal of the Atmospheric Sciences*, Vol. 21, No. 4, July **1964b**, pp. 342–353.

Pedlosky, Joseph, "Finite-Amplitude Baroclinic Waves," *Journal of the Atmospheric Sciences*, Vol. 27, No. 1, Jan. **1970**, pp. 15–30.

Williams, Gareth P., "Thermal Convection in a Rotating Fluid Annulus: Part 1. The Basic Axisymmetric Flow," *Journal of the Atmospheric Sciences*, Vol. 24, No. 2, Mar. **1967a**, pp. 144–161.

Williams, Gareth P., "Thermal Convection in a Rotating Fluid Annulus: Part 2. Classes of Axisymmetric Flow," *Journal of the Atmospheric Sciences*, Vol. 24, No. 2, Mar. **1967b**, pp. 162–174.

Williams, Gareth P., "Numerical Integration of the Three Dimensional Navier-Stokes Equations for Incompressible Flow," *Journal of Fluid Mechanics*, Vol. 37, No. 4, Cambridge, England, July **1969**, pp. 727–750.

Williams, Gareth P., "Baroclinic Annulus Waves," *Journal of Fluid Mechanics*, Vol. 49, No. 3, Cambridge, England, Oct. 15, **1971**, pp. 417–449.